Chemical Science

ROYAL SOCIETY OF CHEMISTRY

EDGE ARTICLE

View Article Online
View Journal | View Issue

Cite this: *Chem. Sci.*, 2026, **17**, 8753

All publication charges for this article have been paid for by the Royal Society of Chemistry

Promoted hydrogen activation and spillover over Pt/Co_3O_4 by facet engineering of Co_3O_4 for enhanced catalytic hydrogenation

Hui Yun, Jiao Feng, Wanying Peng and Mi Xiong *

Received 2nd December 2025
Accepted 6th March 2026

DOI: 10.1039/d5sc09402j

rsc.li/chemical-science

The exposed facets of supported metal catalysts play a crucial role in catalytic hydrogenation performance. However, the internal relationship between the support crystal facet and catalytic performance needs to be further explored. Herein, a series of well-defined Pt/Co_3O_4-x catalysts are fabricated with similar Pt nanoparticle sizes, identical metal loadings, and tailored Co_3O_4 crystal facets (x = o, t, c; where "o", "t", and "c" denote Co_3O_4 exposing predominantly (111), mixed (111)/(100), and (100) facets, respectively). The electronic structure of Pt nanoparticles and the hydrogen spillover capability of Pt/Co_3O_4 are modulated by exposing different crystal facets of Co_3O_4. For the 4-nitrophenol (4-NP) hydrogenation reaction with H_2 as the hydrogen source, the Pt/Co_3O_4-o catalyst with more Pt^0 species and stronger hydrogen spillover capability exhibits the best hydrogenation activity with a turnover frequency (TOF) of 164.2 h^{-1}. Mechanistic studies indicate that, compared with Pt/Co_3O_4-c, the Pt/Co_3O_4-o exhibits weaker adsorption and activation of the nitro group, while its ability to activate H_2 is stronger. The enhanced catalytic activity of Pt/Co_3O_4-o is attributed to promoted hydrogen activation and spillover. This work highlights support crystal facet engineering for regulating the electronic structure and hydrogen spillover effect, which provides in-depth insight into catalyst design and hydrogenation mechanism.

Introduction

Catalytic hydrogenation plays a pivotal role in environmental protection and industrial processes,[1,2] particularly for the degradation of persistent organic pollutants such as 4-nitrophenol (4-NP),[3] a common toxic contaminant in wastewater.[4–6] Supported metal catalysts, especially platinum-based systems, have garnered significant attention due to their exceptional hydrogen activation capability.[7,8] However, the catalytic performance of such systems is intricately linked not only to the active metal sites but also to the structural and electronic properties of the support material.[9–14] Previous extensive research has predominantly focused on elucidating the internal relationship between metal nanoparticle characteristics (including size regulation, alloy composition, and morphological engineering) and the catalytic hydrogenation performance.[15–18]

The microstructures of support, particularly the exposed crystal facet, have been recognized as a critical influencing factor for catalytic hydrogenation performance by modulating the geometric/electronic configurations of metal nanoparticles,[19–22] facilitating support-mediated reactant activation processes,[23,24] inducing interfacial charge transfer dynamics,[25,26] and so on. For example, Gao *et al.* reported a study on tailoring the electronic states of Pd nanoparticles by modulating the exposed crystal facets of ZIF-8 supports.[27] By constructing sandwich-structured ZIF-8_x@Pd@ZIF-8 composites, where distinct facets were engineered, the electron density of Pd nanoparticles was precisely controlled. The (100) facet induced electron-deficient Pd species (ZIF-8_c@Pd@ZIF-8) could preferentially adsorb the electron-rich nitro group of *p*-chloronitrobenzene, achieving excellent catalytic activity and selectivity in the hydrogenation of *p*-chloronitrobenzene to *p*-chloroaniline. Moreover, the facet engineering of nanocatalysts has proven critical for optimizing hydrogen spillover processes for selective hydrogenation. Jiang *et al.* reported a groundbreaking study on tailoring the catalytic performance of highly diluted Pd single-atom catalysts through facet engineering of Cu supports.[28] By dispersing Pd atoms onto Cu nanosheets (exposing (111) facets) and nanocubes (exposing (100) facets), the authors revealed a striking facet-dependent behavior in the semi-hydrogenation of alkynes. While hydrogen spillover occurred on both facets, only Pd_1/Cu(100) exhibited exceptional activity and selectivity even at ultralow Pd loadings (50 ppm). Despite advances in catalyst design, the role of the support facet in modulating electronic states and hydrogen spillover efficiency remains poorly understood.

Herein, we systematically investigate the facet-dependent behavior of Co_3O_4-supported Pt catalysts. Three distinct Co_3O_4 morphologies—octahedral (exposing (111) facets), cubic (exposing (100) facets), and truncated intermediates (co-exposing (111) and (100) facets)—were synthesized to anchor

College of Materials and Chemistry & Chemical Engineering, Chengdu University of Technology, Chengdu 610059, China. E-mail: xiongmi@cdut.edu.cn

Pt nanoparticles with similar sizes and loadings. For the 4-nitrophenol (4-NP) hydrogenation with H_2 as the hydrogen source, the Pt/Co_3O_4-x (x = o, t, c) catalysts present a notable dependence of catalytic activity on exposed facets of supports. And the catalytic activity follows the order: Pt/Co_3O_4-o > Pt/Co_3O_4-t > Pt/Co_3O_4-c. Detailed analyses indicate that, the Pt/Co_3O_4-o with more Pt^0 species has stronger hydrogen activation and spillover capacity and thus significantly accelerates the catalytic hydrogenation performance.

Results and discussion

Catalyst characterization

A series of Co_3O_4 supports with different morphologies were synthesized by hydrothermal method (Fig. S1). Their scanning electron microscopy (SEM) images demonstrate that the synthesized nanoparticles exhibit good morphology (Fig. S2a–c). For different morphologies of Co_3O_4, the corresponding exposed crystal facets are distinct. Specifically, the octahedron Co_3O_4 (Co_3O_4-o) and cube Co_3O_4 (Co_3O_4-c) are enclosed with (111) and (100) facets, respectively, while the truncated octahedron Co_3O_4 (Co_3O_4-t) exposes mixed (111) and (100) facets (Fig. S2d–f). Subsequently, the pre-synthesized Pt nanoparticles were supported on the Co_3O_4-x (x = o, t, c) supports *via* the colloidal deposition method with ~0.3 wt% Pt loading (determined by ICP-OES, Table S1), yielding Pt/Co_3O_4-o, Pt/Co_3O_4-t, and Pt/Co_3O_4-c. SEM images of Pt/Co_3O_4-x (x = o, t, c) show that the size and morphology of the original Co_3O_4-x (x = o, t, c) are almost maintained after Pt loading (Fig. 1a, e, and i).

The high-angle annular dark field scanning transmission electron microscopy (HAADF-STEM) with energy dispersive X-ray spectroscopy (EDS) elemental mapping was further employed to characterize Pt/Co_3O_4-x (x = o, t, c). As shown in Fig. 1b, f, and j, obvious bright spots of Pt nanoparticles are observed. Pt nanoparticles are uniformly dispersed on the Co_3O_4-x (x = o, t, c) supports (Fig. 1c, g, and k). And the average diameters of Pt nanoparticles are similar, about 2.2 nm. Furthermore, the lattice fringes measured in the high-resolution TEM (HRTEM) images of Pt/Co_3O_4-x (x = o, t, c) (Fig. 1d, h and l) are 0.23 nm, corresponding to the (111) planes of Pt. N_2 adsorption–desorption experiments indicate that the Brunauer–Emmett–Teller (BET) surface areas of Pt/Co_3O_4-o, Pt/Co_3O_4-t, and Pt/Co_3O_4-c are 2.4, 3.4, and 3.4 $m^2\ g^{-1}$, respectively, indicating similar surface areas (Table S1).

X-ray diffraction (XRD) was used to investigate the crystal structures of Co_3O_4-x and Pt/Co_3O_4-x (x = o, t, c), as shown in Fig. S3a. All XRD patterns show the diffraction peaks located at 19.0°, 31.3°, 36.9°, 38.6°, 44.9°, 55.7°, 59.4°, and 65.3°, which correspond to the (111), (220), (311), (222), (400), (422), (511), and (440) planes of Co_3O_4, respectively (PDF#43-1003). The intensity ratio of the (111) to (400) peaks for Co_3O_4-x (x = o, t, c) decreases in order of octahedron (0.9) > truncated octahedron (0.7) > cube (0.5) (Fig. S3b), suggesting morphology-dependent facet exposure. Compared to bare Co_3O_4-x (x = o, t, c) supports, the Pt-loaded counterparts (Pt/Co_3O_4-x) exhibit similar trends in the (111)/(400) peak intensity ratios (Fig. S3c), implying that Pt deposition does not significantly perturb the predominant facet distribution of the Co_3O_4 supports. A semi-quantitative analysis based on the XRD intensity ratios estimates the relative abundance of the (111) facet to be ~100%, ~57%, and ~0% for Pt/Co_3O_4-o, -t, and -c, respectively, providing a quantitative structural descriptor for the catalyst series (Table S2). No characteristic diffraction peaks belonging to crystalline Pt nanoparticles are observed, which can be attributed to the low loading and/or small size of Pt species.

X-ray photoelectron spectroscopy (XPS) was employed to reveal the surface chemical states of Pt and Co. Fig. 2a and b show the Co 2p spectra of Co_3O_4-x and Pt/Co_3O_4-x (x = o, t, c), respectively. The peaks at ~780.2 and 795.4 eV are assigned to Co $2p_{3/2}$ and Co $2p_{1/2}$, respectively. The peaks of Co $2p_{3/2}$ can be deconvoluted into two peaks at ~780.0 and 781.4 eV, indicating the coexistence of Co^{3+} and Co^{2+}.[29] Notably, compared to the pristine Co_3O_4-x (x = o, t, c) supports, the Pt-loaded counterparts (Pt/Co_3O_4-x) with the same morphologies show an

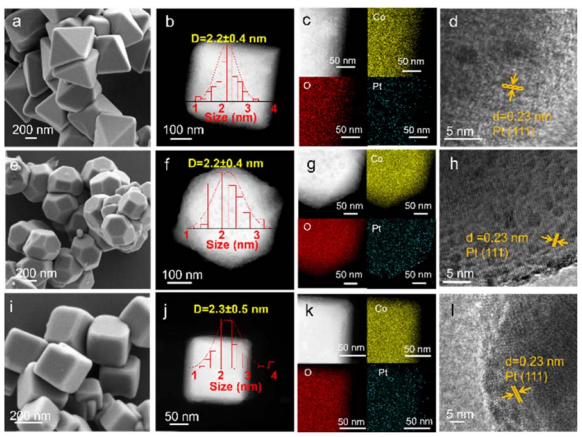

Fig. 1 (a, e, and i) SEM images, (b, f and j) HAADF-STEM images, (c, g, and k) STEM-EDS elemental mappings, and (d, h, and l) HRTEM images of Pt/Co_3O_4-o, Pt/Co_3O_4-t, and Pt/Co_3O_4-c, respectively.

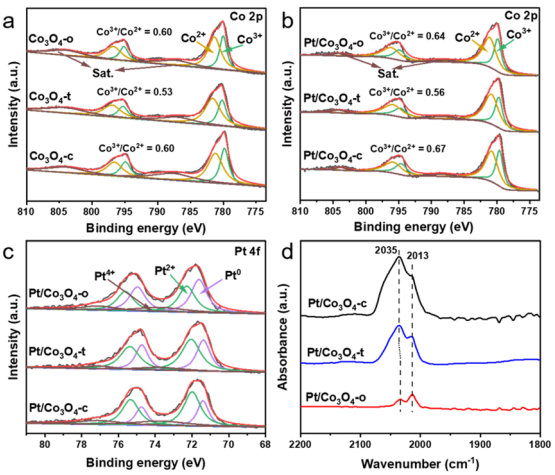

Fig. 2 XPS spectra of Co 2p for (a) Co_3O_4-x and (b) Pt/Co_3O_4-x (x = o, t, c). (c) XPS spectra of Pt 4f and (d) CO-DRIFTS spectra for Pt/Co_3O_4-x (x = o, t, c).

increase in the Co^{3+}/Co^{2+} ratio, implying the transfer of electrons from Co to Pt.[30] Moreover, the XPS spectra of Pt 4f for Pt/Co_3O_4-x (x = o, t, c) show two peaks located at ~71.7 and 75.0 eV, which are attributed to Pt $4f_{7/2}$ and $4f_{5/2}$, respectively (Fig. 2c). And the Pt 4f spectra were fitted by Pt^0, Pt^{2+}, and Pt^{4+}.[31] The fitting results reveal that the Pt^0 content follows the order: Pt/Co_3O_4-o (44.7%) > Pt/Co_3O_4-t (39.4%) > Pt/Co_3O_4-c (26.1%) (Table S3), suggesting the differentiated electronic states of Pt nanoparticles with varied Co_3O_4 facets. To gain insight into the state of Pt under reaction conditions, quasi-in situ XPS analysis was performed after H_2 treatment at 40 °C. Intriguingly, although the Pt^0 content increased for all catalysts, the facet-dependent order remained unchanged (Fig. S4, Table S3), suggesting that the intrinsic electronic modulation by the support facet is preserved under a reducing atmosphere.

Further, diffuse-reflectance infrared Fourier transform spectroscopy (DRIFTS) of CO chemisorption was performed to evaluate the electronic states of surface Pt species in Pt/Co_3O_4-x (x = o, t, c), as shown in Fig. 2d. Two absorption bands observed at 2033–2035 and 2013 cm^{-1} are assigned to the linear absorption of CO on the terrace and step sites of Pt nanoparticles, respectively.[32] Compared to the Pt/Co_3O_4-t and Pt/Co_3O_4-c, the CO adsorption peak at the terrace sites of Pt/Co_3O_4-o shifts to a lower wavenumber (from 2035 to 2033 cm^{-1}). Additionally, the relative intensity of the CO signal adsorbed at the step sites follows the order: Pt/Co_3O_4-o > Pt/Co_3O_4-t > Pt/Co_3O_4-c. These results suggest that the Pt species on Pt/Co_3O_4-o surfaces are in a lower valence state,[33] which aligns with the XPS result. The observed charge transfer and modified electronic state of Pt (Fig. 2) confirm that a facet-dependent metal-support interaction is effectively established through our colloidal deposition process, even in the absence of high-temperature treatment.

Hydrogen temperature-programmed reduction (H_2-TPR) was carried out to investigate the reducibility of Co_3O_4-x and Pt/Co_3O_4-x (x = o, t, c), as shown in Fig. 3a and b. H_2-TPR profiles show no reduction peak below 100 °C for any Pt/Co_3O_4-x catalyst, confirming the metallic state (Pt^0) of the pre-synthesized nanoparticles. The prominent peaks observed at higher temperatures (~370 °C) are therefore attributed solely to the reduction of the Co_3O_4 support. The shift to lower temperatures (by ~50 °C) compared to bare Co_3O_4 demonstrates that metallic Pt^0 promotes support reduction *via* hydrogen spillover.[34,35]

To detect spilled hydrogen, hydrogen temperature-programmed desorption coupled with mass spectrometry (H_2-TPD-MS) measurements of Pt/Co_3O_4-x were performed. As shown in Fig. 3c and S5, the MS signals reveal that the major desorption products are H_2O ($m/z = 18$) and OH species ($m/z = 17$), with no significant molecular H_2 ($m/z = 2$) detected. This indicates that active hydrogen species generated on Pt^0 sites spill over onto the Co_3O_4 support and react with lattice oxygen to form surface hydroxyl groups, which subsequently recombine and decompose upon heating.[36,37] The profiles show two main desorption regions: a peak at ~280 °C attributed to the removal of weakly-bound hydroxyls, and another more intense peak at ~650 °C associated with strongly-bound hydroxyls likely formed from hydrogen that has migrated deeper into the oxide lattice. Critically, the intensity of the high-temperature peak follows the order: Pt/Co_3O_4-o > Pt/Co_3O_4-t > Pt/Co_3O_4-c. This provides direct evidence that the (111) facet of Co_3O_4 is the most effective in stabilizing and incorporating spilled hydrogen.

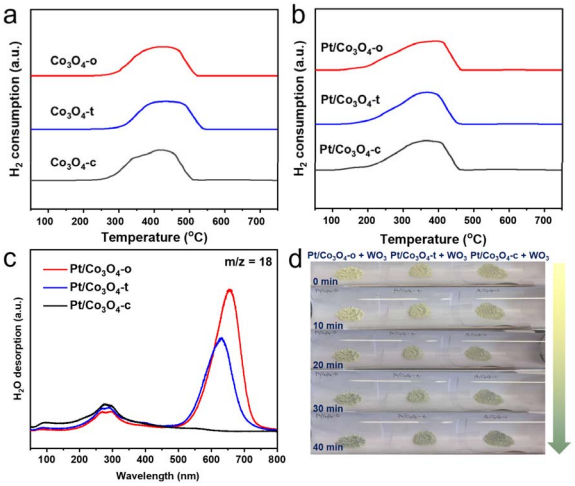

Fig. 3 H_2-TPR profiles of (a) the as-prepared Co_3O_4-x and (b) Pt/Co_3O_4-x (x = o, t, c) catalysts. (c) H_2-TPD profiles of the as-prepared Pt/Co_3O_4-x (x = o, t, c). (d) Photographs of samples made with WO_3 (300 mg) mixed with the Pt/Co_3O_4-x (x = o, t, c) catalysts (1 mg) before treatment and after treatment with 10% H_2/Ar at 25 °C for different times.

Further, a color change experiment was conducted to visually evaluate the hydrogen spillover effect (Fig. 3d). By mixing 1 mg of Pt/Co_3O_4-x catalysts and 300 mg of WO_3 nanowires, the original color of the mixtures is light yellow. After being exposed to hydrogen atmosphere, the mixture of Pt/Co_3O_4-o and WO_3 exhibits the most pronounced color change within 40 minutes, implying the strongest hydrogen spillover effect over Pt/Co_3O_4-o. This result aligns with the H_2-TPD-MS data and is attributed to the stronger metal-support interaction in Pt/Co_3O_4-o, which facilitates the generation and transfer of active hydrogen species (Fig. 2c and d and S6). Further, a parallel experiment conducted in aqueous reaction conditions (Fig. S7) also yielded a distinct color change, confirming that hydrogen spillover persists in the liquid environment relevant to catalysis.

Catalytic performance of Pt/Co_3O_4-x (x = o, t, c) for 4-NP hydrogenation

The catalytic performance of Pt/Co_3O_4-x (x = o, t, c) was evaluated by the 4-NP reduction. The reduction process using H_2 as hydrogen source was monitored by UV-vis spectroscopy every ten minutes, and the intensity of the UV absorption peak at 400 nm was used to quantify the concentration of 4-NP. As shown in Fig. 4a–c, the peak intensity at 400 nm gradually decreased as the reaction proceeded. Simultaneously, a new peak appeared at 257 nm, which was ascribed to the formation of 4-aminobenzenol (4-AP) (Fig. S8). Among the Pt/Co_3O_4-o, Pt/Co_3O_4-t, and Pt/Co_3O_4-c catalysts, the Pt/Co_3O_4-o exhibited the shortest reaction time with nearly 100% conversion (Fig. S9). Furthermore, Fig. 4d shows a logarithmic plot of the

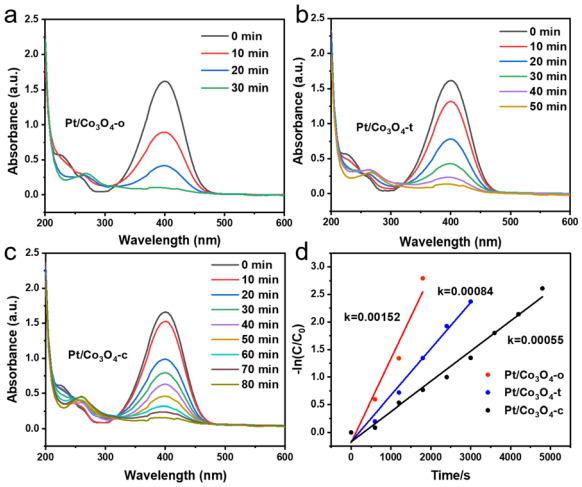

Fig. 4 Time-dependent UV-vis spectra of 4-NP reduced by (a) Pt/Co_3O_4-o, (b) Pt/Co_3O_4-t, and (c) Pt/Co_3O_4-c. (d) The kinetics plots of $-\ln(C/C_0)$ against the reaction time for the reduction of 4-NP over different Pt/Co_3O_4-x (x = o, t, c) catalysts.

concentration ($-\ln(C/C_0)$ *versus* reaction time for different catalysts. The concentration ($-\ln(C/C_0)$ is proportional to the reaction time, and thus the apparent kinetic rate constant (k_{app}) can be estimated based on slope regression of the logarithmic graph ($\ln(C_t/C_0) = -k_{app}t$).[38] Compared to the Pt/Co_3O_4-t and Pt/Co_3O_4-c catalysts (8.4×10^{-4} and 5.5×10^{-4} s^{-1}, respectively), the Pt/Co_3O_4-o has the highest k_{app} value (1.52×10^{-3} s^{-1}), indicating its superior catalytic activity. Under identical reaction conditions, the bare Co_3O_4 support exhibited negligible catalytic activity (Fig. S10).

To further evaluate the intrinsic activity per Pt site, the turnover frequency (TOF) was determined based on CO chemisorption measurements. The calculated TOF values follow the same trend: Pt/Co_3O_4-o (164.2 h^{-1}) > Pt/Co_3O_4-t (115.2 h^{-1}) > Pt/Co_3O_4-c (75.6 h^{-1}) (Table S4). Subsequently, the apparent activation energy (E_a) experiment was performed (Fig. S11). The E_a values follow the order: Pt/Co_3O_4-o (23.0 kJ mol^{-1}) < Pt/Co_3O_4-t (25.3 kJ mol^{-1}) < Pt/Co_3O_4-c (55.2 kJ mol^{-1}). The significantly lower E_a for Pt/Co_3O_4-o accounts for its superior catalytic activity. More importantly, we establish a quantitative correlation between the Co_3O_4(111) facet exposure and the TOF (Fig. S12). This linear correlation directly demonstrates that the abundance of the (111) facet is the predominant factor governing the catalytic hydrogenation activity.

For comparison, control catalysts were also prepared *via* a conventional impregnation-chemical reduction method. While the same activity order (Pt/Co_3O_4-o > Pt/Co_3O_4-c) was preserved, the catalytic activities of the impregnation-prepared catalysts were substantially lower than their colloidal-deposition counterparts (Fig. S13). This lower activity is consistent with the larger and less uniform Pt nanoparticles formed by the impregnation method (Fig. S14), demonstrating the advantage of the colloidal deposition route for achieving high Pt dispersion on our low-surface-area Co_3O_4 supports.

The Pt/Co_3O_4-o was reused to test the stability for 4-NP hydrogenation. The catalytic activity was well maintained after five cycles (Fig. S15), indicating its high catalytic stability. Post-reaction characterizations (XRD, TEM, and XPS) confirm that the Pt nanoparticle size, dispersion, and chemical state, as well as the Co_3O_4 crystal facets, remain essentially unchanged after cycling (Fig. S16 and Table S3). Together with the minimal Pt leaching (<0.2%) confirmed by ICP-MS (Table S5), these results demonstrate the robust structural and compositional stability of the catalyst. When nitrobenzene was employed as the substrate, the Pt/Co_3O_4-o still exhibited the superior catalytic activity (Fig. S17 and S18).

Compared with state-of-the-art catalysts for 4-NP hydrogenation (Table S6), the optimal Pt/Co_3O_4-o demonstrates a competitive turnover frequency (164.2 h^{-1}) under an exceptionally mild condition (40 °C, 1 bar H_2). Many reported systems require significantly higher H_2 pressures or temperatures to achieve comparable activity. This combination of high intrinsic activity, low activation barrier, robust stability, and facet-dependent performance underscores the practical promise and fundamental insight offered by our facet-engineered catalyst.

Catalytic mechanism

To elucidate the origin of the superior catalytic performance of Pt/Co_3O_4-o, diffuse reflectance infrared Fourier transform spectroscopy (DRIFTS) was first used to investigate the adsorption behavior of 4-NP on Pt/Co_3O_4-o and Pt/Co_3O_4-c as model catalysts, as shown in Fig. S19. The spectra of Pt/Co_3O_4-o and Pt/Co_3O_4-c show two bands at 1578 and 1316 cm^{-1}, corresponding to asymmetric stretching and symmetric stretching vibrations of the nitro group, respectively.[39] Compared with the Pt/Co_3O_4-c catalyst, Pt/Co_3O_4-o exhibits a weaker peak intensity at 1578 cm^{-1}, suggesting a weaker adsorption capability for the nitro group. Further, the adsorption and activation capability of Pt/Co_3O_4-o and Pt/Co_3O_4-c for 4-NP and H_2 was explored through kinetic experiments. Fig. 5a displays the kinetic behavior for 4-NP adsorption and activation. The reaction order with respect to 4-NP is higher for Pt/Co_3O_4-o (0.81) than for Pt/Co_3O_4-c (0.75), implying that it is more difficult for Pt/Co_3O_4-o to activate the nitro group. This is consistent with the result of DRIFTS. For the adsorption and activation of H_2 (Fig. 5b), the reaction order of Pt/Co_3O_4-o (0.41) is lower than that of Pt/Co_3O_4-c (0.53), indicating that it is easier for Pt/Co_3O_4-o to activate H_2.

To gain theoretical insight, DFT calculations were conducted. Pt_4 clusters supported on Co_3O_4-(111) and Co_3O_4-(100) (labeled as Pt_4/Co_3O_4-(111) and Pt_4/Co_3O_4-(100), respectively) were constructed to mimic the Pt/Co_3O_4-o and Pt/Co_3O_4-c catalysts based on the distinct exposed facets of Co_3O_4 supports: the octahedral Co_3O_4-o predominantly exposes the (111) facet, whereas the cubic Co_3O_4-c preferentially exposes the (100) facet (Fig. S20a and b). First, when Pt_4 clusters were anchored on different Co_3O_4 model surfaces, the electron transfer from Co_3O_4 to Pt_4 was about $-1.65|e|$ for Pt_4/Co_3O_4-(111) and $-0.74|e|$ for Pt_4/Co_3O_4-(100), respectively (Fig. S20c and d, Table S7). The

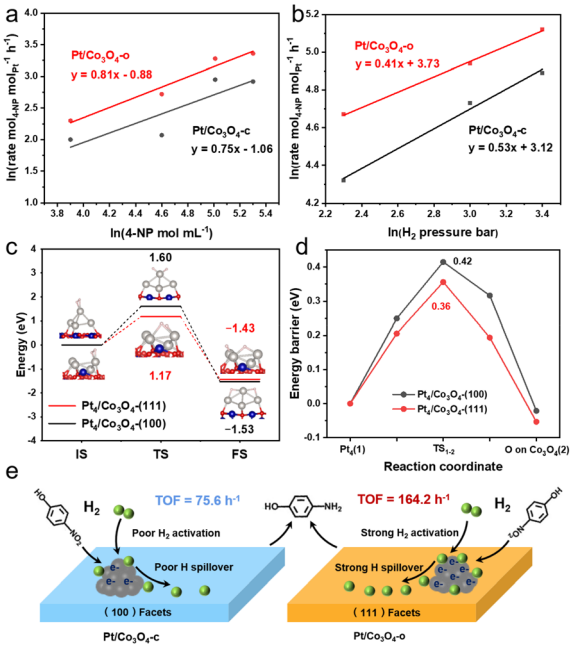

Fig. 5 Kinetic experiments of 4-NP hydrogenation over the Pt/Co_3O_4-o and Pt/Co_3O_4-c catalysts: the reaction order for (a) 4-NP and (b) H_2. The reaction rates were determined at conversions below 30%. (c) Potential energy profiles of H_2 dissociation on the Pt_4/Co_3O_4-(100) and Pt_4/Co_3O_4-(111) model surfaces. (d) Potential energy profiles for hydrogen atom migration from Pt_4 to Co_3O_4 across the interface on the Pt_4/Co_3O_4-(100) and Pt_4/Co_3O_4-(111) model surfaces. (e) Schematic illustration of possible mechanisms on Pt/Co_3O_4-c and Pt/Co_3O_4-o for 4-NP hydrogenation.

charge density differences indicate that more electrons transfer from Co_3O_4 to Pt for Pt_4/Co_3O_4-(111), leading to a lower oxidation state of Pt. This is also confirmed by the XPS results. Next, Fig. S21a–d shows the optimized adsorption structures of 4-NP on the Pt_4/Co_3O_4-(111) and Pt_4/Co_3O_4-(100) surfaces. The adsorption energy results presented in Fig. S21e indicate that the Pt_4/Co_3O_4-(111) exhibits the weaker capability for facilitating the nitro group activation. Further, Fig. 5c reveals the adsorption and activation of H_2 on the Pt_4/Co_3O_4-(111) and Pt_4/Co_3O_4-(100) surfaces, in which the energy barrier (1.17 eV) of H_2 dissociation on Pt_4/Co_3O_4-(111) is lower than that on Pt_4/Co_3O_4-(100) (1.6 eV), implying that the activation of H_2 by Pt_4/Co_3O_4-(111) is easier. These results are consistent with the kinetics results. Furthermore, for hydrogen-atom migration from Pt to Co_3O_4 across the interface, the energy barrier on the Pt_4/Co_3O_4-(111) (0.36 eV) is lower than that on the Pt_4/Co_3O_4-(100) (0.42 eV), indicating kinetically more favourable hydrogen spillover on Co_3O_4-(111) (Fig. 5d and S22).

Based on the above results, the possible promotion mechanism is proposed (Fig. 5e). For the hydrogenation reaction, the activity of a catalyst is strongly related to the substrate activation ability, H_2 activation ability, as well as active hydrogen spillover.[40,41] With Pt/Co_3O_4-o and Pt/Co_3O_4-c as model catalysts, the kinetic experiments and DFT calculations illustrate that compared with Pt/Co_3O_4-c, the adsorption/activation of 4-NP on the Pt/Co_3O_4-o is weaker, indicating that the adsorption/activation of 4-NP is not the key factor contributing to the difference in activity in this reaction. However, the Pt/Co_3O_4-o has a stronger H_2 dissociation ability and lower hydrogen-migration barrier. The accelerated hydrogen dissociation on electron-rich Pt sites, coupled with enhanced hydrogen spillover to the Co_3O_4 support, establishes a dynamic hydrogen supply chain that maximizes the utilization of active hydrogen species. The 4-NP adsorbed on Pt or near Pt-Co_3O_4 interfaces can continuously consume active hydrogen species, and the hydrogenation reaction can be promoted in a dynamic process.

Conclusions

In summary, a series of well-defined Pt/Co_3O_4-x (x = o, t, c) catalysts with tailored Co_3O_4 crystal facets have been successfully constructed for the hydrogenation of 4-nitrophenol. Owing to the crystal facet effect, the Pt nanoparticles in Pt/Co_3O_4-o are more negatively charged than those in Pt/Co_3O_4-c and Pt/Co_3O_4-t, and Pt/Co_3O_4-o exhibits the strongest hydrogen spillover capability. For the 4-nitrophenol (4-NP) hydrogenation reaction, the Pt/Co_3O_4-o has the best catalytic activity with a TOF value of 164.2 h^{-1}. Detailed analyses reveal that the negatively charged Pt sites are favorable to the activation of hydrogen rather than the nitro group. Therefore, the enhanced catalytic activity of Pt/Co_3O_4-o is attributed to the promoted hydrogen activation and spillover. This work highlights crystal facet engineering of support to regulate the electronic structure and hydrogen spillover effect, which provides in-depth insight into the catalyst design and hydrogenation mechanism.

Author contributions

The manuscript was written through contributions of all authors. All authors have given approval to the final version of the manuscript. Hui Yun: investigation, validation, visualization, data curation, formal analysis, methodology, writing – original draft. Jiao Feng: visualization, writing – review & editing. Wanying Peng: visualization, writing – review & editing. Mi Xiong: conceptualization, funding acquisition, supervision, writing – review & editing.

Conflicts of interest

There are no conflicts to declare.

Data availability

The data supporting this article has been included as part of the supplementary information (SI). Supplementary information is available. See DOI: https://doi.org/10.1039/d5sc09402j.

Acknowledgements

We acknowledge the financial support from the National Natural Science Foundation of China (22302022), the Natural Science Foundation of Sichuan Province (24NSFSC4428), and

the Cheng du University of Technology Teachers Development Research Fund (10912-KYQD2022-09565).

References

1 D. Wang and D. Astruc, The Golden Age of Transfer Hydrogenation, *Chem. Rev.*, 2015, **115**, 6621–6686.
2 A. V. Karim, Ł. Cichocki, C. Wang and G. Boczkaj, Advanced reduction processes (ARPs) based on catalytic hydrogenation for wastewater pollutants degradation - a special focus on process efficiency and mechanisms – a review, *J. Cleaner Prod.*, 2025, **531**, 146870.
3 S. Luo, Z. Liu, Y. Liu, E. Almatrafi, B. Shao, B. Song, C. Zhou, Y. Fu, M. He, Z. Zeng and G. Zeng, Versatile CMPs as platforms to support Ag nanocatalysts for nitrophenol hydrogenation in continuous flow-through process, *Chem. Eng. J.*, 2022, **442**, 136207.
4 B. Lai, Z. Chen, Y. Zhou, P. Yang, J. Wang and Z. Chen, Removal of high concentration p-nitrophenol in aqueous solution by zero valent iron with ultrasonic irradiation (US-ZVI), *J. Hazard. Mater.*, 2013, **250–251**, 220–228.
5 B. Lai, Y. H. Zhang, R. Li, Y. X. Zhou and J. Wang, Influence of operating temperature on the reduction of high concentration p-nitrophenol (PNP) by zero valent iron (ZVI), *Chem. Eng. J.*, 2014, **249**, 143–152.
6 Y. Ren, J. Li, L. Lai and B. Lai, Premagnetization enhancing the reactivity of Fe^0/(passivated Fe^0) system for high concentration p-nitrophenol removal in aqueous solution, *Chemosphere*, 2017, **197**, 634–643.
7 Y. Zhang and J. Zhou, Synergistic catalysis by a hybrid nanostructure Pt catalyst for high-efficiency selective hydrogenation of nitroarenes, *J. Catal.*, 2021, **395**, 445–456.
8 Q. Zhang, J. Bu, J. Wang, C. Sun, D. Zhao, G. Sheng, X. Xie, M. Sun and L. Yu, Highly Efficient Hydrogenation of Nitrobenzene to Aniline over Pt/CeO_2 Catalysts: The Shape Effect of the Support and Key Role of Additional Ce^{3+} Sites, *ACS Catal.*, 2020, **10**, 10350–10363.
9 Y. Wang, C. Wang, L. Wang, L. Wang and F. S. Xiao, Zeolite Fixed Metal Nanoparticles: New Perspective in Catalysis, *Acc. Chem. Res.*, 2021, **54**, 2579–2590.
10 G. Pacchioni and H. J. Freund, Controlling the charge state of supported nanoparticles in catalysis: lessons from model systems, *Chem. Soc. Rev.*, 2018, **47**, 8474–8502.
11 T. W. van Deelen, C. Hernández Mejía and K. P. de Jong, Control of metal-support interactions in heterogeneous catalysts to enhance activity and selectivity, *Nat. Catal.*, 2019, **2**, 955–970.
12 M. Xiong, Y. Li, L. Sun, Q. Hu, Z. Lv, S. Xing, H. Yun, S. Zhang and Z. Gao, Magnetically recyclable bimetallic Pt-Co/CoO catalyst derived through hydrogen spillover for fast hydrogen release through ammonia borane hydrolysis, *Surf. Interfaces*, 2025, **62**, 106242.
13 P. Zhang, T. Qin, D. Li, X. Q. Wu, Y. X. Ma, H. Q. Guo, J. Xiong, X. Liu, Z. Zhao, L. W. Chen, J. Liu and Y. C. Wei, Temperature-induced evolution of CuO_x clusters in CuO_x/TiO_2 catalyst for boosting auto-exhaust oxidation, *Appl. Catal. B Environ. Energy*, 2025, **361**, 124674.
14 Y. F. Li, T. Qin, Y. C. Wei, J. Xiong, P. Zhang, K. Z. Lai, H. J. Chi, X. Liu, L. W. Chen, X. L. Yu, Z. Zhao, L. N. Li and J. Liu, A single site ruthenium catalyst for robust soot oxidation without platinum or palladium, *Nat. Commun.*, 2023, **14**, 7149.
15 M. Ahmadi, H. Mistry and B. Roldan Cuenya, Tailoring the Catalytic Properties of Metal Nanoparticles via Support Interactions, *J. Phys. Chem. Lett.*, 2016, **7**, 3519–3533.
16 Z. Li, S. Ji, Y. Liu, X. Cao, S. Tian, Y. Chen, Z. Niu and Y. Li, Well-Defined Materials for Heterogeneous Catalysis: From Nanoparticles to Isolated Single-Atom Sites, *Chem. Rev.*, 2019, **120**, 623–682.
17 L. Liu and A. Corma, Metal Catalysts for Heterogeneous Catalysis: From Single Atoms to Nanoclusters and Nanoparticles, *Chem. Rev.*, 2018, **118**, 4981–5079.
18 X. Liu, X. Wang, S. Zhen, G. Sun, C. Pei, Z. J. Zhao and J. Gong, Support stabilized PtCu single-atom alloys for propane dehydrogenation, *Chem. Sci.*, 2022, **13**, 9537–9543.
19 X. Huang, C. Dang, H. Yu, H. Wang and F. Peng, Morphology Effect of Ir/$La_2O_2CO_3$ Nanorods with Selectively Exposed {110} Facets in Catalytic Steam Reforming of Glycerol, *ACS Catal.*, 2015, **5**, 1155–1163.
20 Z. Hu, Z. Zou, A. Xie, C. Chen, X. Zhu, Y. Zhang, H. Zhang, H. Zhao and G. Wang, Crystal plane effect of ceria on supported copper catalyst for liquid-phase hydrogenation of unsaturated aldehyde, *J. Colloid Interface Sci.*, 2021, **596**, 34–43.
21 P. Zhang, J. Xiong, Y. C. Wei, Y. F. Li, Y. L. Zhang, J. J. Tang, W. Y. Song, Z. Zhao and J. Liu, Exposed {001} facet of anatase TiO_2 nanocrystals in Ag/TiO_2 catalysts for boosting catalytic soot combustion: The facet-dependent activity, *J. Catal.*, 2021, **398**, 109–122.
22 S. Wang, C. Liu, W. Hao, Y. Zhuang, J. Chen, X. Zhu, L. Wang, X. Niu, J. Mao, D. Ma and Q. Zhao, Structural evolution of metal single-atoms and clusters in catalysis: Which are the active sites under operative conditions?, *Chem. Sci.*, 2025, **16**, 6203–6218.
23 M. Cargnello, V. V. T. Doan-Nguyen, T. R. Gordon, R. E. Diaz, E. A. Stach, R. J. Gorte, P. Fornasiero and C. B. Murray, Control of Metal Nanocrystal Size Reveals Metal-Support Interface Role for Ceria Catalysts, *Science*, 2013, **341**, 771–773.
24 G. Huang, Q. H. Yang, Q. Xu, S. H. Yu and H. L. Jiang, Polydimethylsiloxane Coating for a Palladium/MOF Composite: Highly Improved Catalytic Performance by Surface Hydrophobization, *Angew. Chem., Int. Ed.*, 2016, **55**, 7379–7383.
25 Q. Fu and T. Wagner, Interaction of nanostructured metal overlayers with oxide surfaces, *Surf. Sci. Rep.*, 2007, **62**, 431–498.
26 J. F. Zhou, B. Peng, M. Ding, B. Q. Shan, Y. S. Zhu, L. Bonneviot, P. Wu and K. Zhang, The nature of crystal facet effect of TiO_2-supported Pd/Pt catalysts on selective hydrogenation of cinnamaldehyde: electron transfer process promoted by interfacial oxygen species, *Phys. Chem. Chem. Phys.*, 2024, **26**, 18854–18864.

27 M. L. Gao, L. Li, Z. X. Sun, J. R. Li and H. L. Jiang, Facet Engineering of a Metal-Organic Framework Support Modulates the Microenvironment of Palladium Nanoparticles for Selective Hydrogenation, *Angew. Chem., Int. Ed.*, 2022, **61**, e202211216.

28 L. Jiang, K. Liu, S. F. Hung, L. Zhou, R. Qin, Q. Zhang, P. Liu, L. Gu, H. M. Chen, G. Fu and N. Zheng, Facet engineering accelerates spillover hydrogenation on highly diluted metal nanocatalysts, *Nat. Nanotechnol.*, 2020, **15**, 848–854.

29 Z. Cai, Y. Bi, E. Hu, W. Liu, N. Dwarica, Y. Tian, X. Li, Y. Kuang, Y. Li, X. Q. Yang, H. Wang and X. Sun, Single-Crystalline Ultrathin Co_3O_4 Nanosheets with Massive Vacancy Defects for Enhanced Electrocatalysis, *Adv. Energy Mater.*, 2017, **8**, 1701694.

30 Z. Li, T. He, D. Matsumura, S. Miao, A. Wu, L. Liu, G. Wu and P. Chen, Atomically Dispersed Pt on the Surface of Ni Particles: Synthesis and Catalytic Function in Hydrogen Generation from Aqueous Ammonia–Borane, *ACS Catal.*, 2017, **7**, 6762–6769.

31 H. Jeong, D. Shin, B. S. Kim, J. Bae, S. Shin, C. Choe, J. W. Han and H. Lee, Controlling the Oxidation State of Pt Single Atoms for Maximizing Catalytic Activity, *Angew. Chem., Int. Ed.*, 2020, **59**, 20691–20696.

32 J. Zhang, Y. Pan, D. Feng, L. Cui, S. Zhao, J. Hu, S. Wang and Y. Qin, Mechanistic insight into the synergy between platinum single atom and cluster dual active sites boosting photocatalytic hydrogen evolution, *Adv. Mater.*, 2023, **35**, 2300902.

33 T. Zhang, J. Jin, J. Chen, Y. Fang, X. Han, J. Chen, Y. Li, Y. Wang, J. Liu and L. Wang, Pinpointing the axial ligand effect on platinum single-atom-catalyst towards efficient alkaline hydrogen evolution reaction, *Nat. Commun.*, 2022, **13**, 6875.

34 J. Zhang, W. Chen, H. Ge, C. Chen, W. Yan, Z. Gao, J. Gan, B. Zhang, X. Duan and Y. Qin, Synergistic effects in atomic-layer-deposited PtCox/CNTs catalysts enhancing hydrolytic dehydrogenation of ammonia borane, *Appl. Catal. B Environ. Energy*, 2018, **235**, 256–263.

35 B. Ouyang, S. Xiong, Y. Zhang, B. Liu and J. Li, The study of morphology effect of Pt/Co_3O_4 catalysts for higher alcohol synthesis from CO_2 hydrogenation, *Appl. Catal., A*, 2017, **543**, 189–195.

36 H. Li, M. Abdelgaid, J. R. Paudel, N. P. Holzapfel, V. Augustyn, J. R. McKone, G. Mpourmpakis and E. J. Crumlin, Operando unveiling of hydrogen spillover mechanisms on tungsten oxide surfaces, *J. Am. Chem. Soc.*, 2025, **147**, 6472–6479.

37 Y. Liu, R. Zhang, L. Lin, Y. Wang, C. Liu, R. Mu and Q. Fu, Direct observation of accelerating hydrogen spillover via surface-lattice-confinement effect, *Nat. Commun.*, 2023, **14**, 613.

38 Z. Cheng, B. He and L. Zhou, A general one-step approach for in situ decoration of MoS_2 nanosheets with inorganic nanoparticles, *J. Mater. Chem. A*, 2015, **3**, 1042–1048.

39 H. Feng, Y. Yang, Y. Niu, L. Wang, P. Yin, S. Hong, B. Zhang, X. Zhang and M. Wei, Highly-efficient RuNi single-atom alloy catalysts toward chemoselective hydrogenation of nitroarenes, *Nat. Commun.*, 2022, **13**, 3188.

40 Z. Zhao, X. Li, X. Liu, H. Gao, A. Jia, S. Xie, X. Song, X. Liu, F. Yang and Q. Yang, $Pt/Fe\text{-}TiO_2$-Catalyzed Selective Carbonyl Hydrogenation: Fe-Promoted Hydrogen Spillover, *ACS Catal.*, 2024, **14**, 4478–4488.

41 L. Xie, J. Liang, L. Jiang and W. Huang, Effects of oxygen vacancies on hydrogenation efficiency by spillover in catalysts, *Chem. Sci.*, 2025, **16**, 3408–3429.